nature communications

Article

https://doi.org/10.1038/s41467-025-56010-w

Elliptical ejecta of asteroid Dimorphos is due to its surface curvature

Received: 17 November 2023

Accepted: 6 January 2025

Published online: 14 February 2025

Check for updates

A list of authors and their affiliations appears at the end of the paper

Kinetic deflection is a planetary defense technique delivering spacecraft momentum to a small body to deviate its course from Earth. The deflection efficiency depends on the impactor and target. Among them, the contribution of global curvature was poorly understood. The ejecta plume created by NASA's Double Asteroid Redirection Test impact on its target asteroid, Dimorphos, exhibited an elliptical shape almost aligned along its north-south direction. Here, we identify that this elliptical ejecta plume resulted from the target's curvature, reducing the momentum transfer to 44 ± 10% along the orbit track compared to an equivalent impact on a flat target. We also find lower kinetic deflection of impacts on smaller near-Earth objects due to higher curvature. A solution to mitigate low deflection efficiency is to apply multiple low-energy impactors rather than a single high-energy impactor. Rapid reconnaissance to acquire a target's properties before deflection enables determining the proper locations and timing of impacts.

Planetary defense is an international effort to mitigate threats of small-body collisions with Earth[1,2]. Among its key planetary defense technologies is kinetic deflection, in which a spacecraft collides with a hazardous body to change its trajectory and eliminate or reduce the risk of its impact on Earth[3]. Kinetic deflection is a practical approach when targets are less than about 250 m in radius if the encounter with Earth is several decades in the future[1–4]. In contrast, near-Earth objects (NEOs) less than 50 m in radius are the most probable threat and high-priority targets for rapid reconnaissance flyby missions[1–4]. The momentum transfer enhancement factor, known as β, is a well-used parameter, in its simplest form, the total momentum imparted to the target by the spacecraft and ejecta normalized by its momentum before impact[5–7]. Recent impact physics studies suggest the dependence of β on the impactor's properties and orientation and the target's composition and strength[8–15]. Local topography is another contributor to kinetic deflection. When the crater formation is at a local scale on the target body, momentum transfer is only affected by local topography[11,16–19]. From a tactical perspective, imparting higher kinetic energy is preferred to maximize deflecting the target[1–4]. However, when a higher kinetic energy impact generates a larger impact crater relative to the target body, the target's global curvature becomes important to the excavation process[20]. How a target's global curvature controls kinetic deflection remains unexplored.

Without the context of planetary defense, two previous spacecraft missions conducted relatively small impact experiments compared to the sizes of their target bodies. NASA's Deep Impact mission targeted Comet 9P/Tempel 1, a Jupiter family comet about 6 km across[21]. The impacting spacecraft, with a mass of 364 kg at an impact speed of 10.3 km/s collided with this cometary nucleus[21] and produced a crater with a radius of 100 ± 10 m[22], which is only 4% of the comet's equivalent radius. Deep Impact suggests the strong dependence of ejecta plume geometry and morphology on impact obliquity and target properties at a local scale[23–25]. Similarly, JAXA's Hayabusa2 mission conducted a Small Carry-on Impactor (SCI) experiment on the carbonaceous asteroid (162173) Ryugu[26]. The 2 kg copper projectile impacted at a speed of 2 km/s, creating a 7.3 m radius crater (only 2% of the asteroid's equivalent radius); it appears that ejecta formation was affected by the presence of a large boulder beneath the impact site[26,27]. These impacts were too small to impart significant momentum transfer at a realistic scale for planetary defense and be affected by their targets' global curvatures.

NASA's Double Asteroid Redirection Test (DART) mission was the first full-scale planetary defense demonstration mission that deliberately crashed a spacecraft into Dimorphos, the smaller satellite of the binary system (65803) Didymos[28,29]. On September 26, 2022, at 23: 14: 24 UTC, the DART spacecraft (579 kg at the time of impact) successfully impacted at 8.84° S and 264.30° E on Dimorphos in the body's fixed

e-mail: thirabayashi@gatech.edu

frame (ISU_DIMORPHOS) with an impact speed of 6.145 km/s[28,29]. The spatial extent of the pre-impact Dimorphos was 179 m × 169 m × 115 m, indicating a relatively oblate shape[30]. This impact caused a mutual orbit period change of Dimorphos relative to Didymos of $-33.0 \pm 1.0(3\sigma)$ min[31]. After the collision, the ejecta plume evolved with time, exhibiting a cone-like shape that grew initially but later decayed gradually, a major part of which joined as part of the tail mainly driven by solar radiation pressure[32–44]. β estimates ranged between 2.2 and 4.9 (depending on the assumed bulk density of the asteroid, which remains unknown but will be constrained by ESA's Hera mission[45]); for a bulk density of 2.4 g/cc, β was determined to be $3.61^{+0.19}_{-0.25}$[46].

Here, we show in detail the contributions of an asteroid's global curvature to kinetic deflection by using the recently obtained data from DART. Measuring the geometry of the DART impact-driven ejecta first applies images taken by Hubble Space Telescope (HST)[40] and the Light Italian Cubesat for Imaging of Asteroids (LICIACube)'s camera, LUKE (LICIACube Unit Key Explorer)[41,42]. The contribution of Dimorphos's global curvature to the DART momentum transfer is determined using the measured cone geometry. Furthermore, an analysis applies an established approach for the DART impact case to interpret the global curvature's contribution to kinetic deflection for NEOs less than 50 m in radius.

Results

Ejecta cone geometry

The cone geometry measurement applies images taken by HST and LICIACube, extending earlier efforts: those using LUKE images only[42] and HST images only[40,46] with the assumption of circular cone geometry, and those using LUKE images only to constrain the elliptical cone geometry[47]. The present approach differs from theirs, using both HST and LICIACube images. The results are consistent with theirs but give the uncertainties of the elliptical cone geometry, which is critical for the following momentum transfer computation.

The parameters describing the cone geometry include the wide-cone opening angle, θ_1, the narrow-cone opening angle, θ_2, the azimuthal angle from Dimorphos's north at the impact site defining the wide-cone orientation, ϕ, and the cone axis direction described using Right Ascension, *RA*, and Declination, *DEC* (Fig. 1). The J2000 International Celestial Reference System (later known as J2000) is the baseline coordinate frame defining the cone axis direction, *RA* and *DEC*. The analysis uses a time range at 160–195 s after the impact (T + 160–195 s) within a distance of a few kilometers from Dimorphos's surface (i.e., LICIACube images) and, equivalently, at T + 0.41–8.2 h within a few hundred kilometers (i.e., HST images). The ejecta cone geometry observed by both HST and LICIACube consists of particles with consistent ejection speeds of 0.5–20 m/s. Applying these durations comes from the timing of LICIACube's closest approach (CA) with Dimorphos at T + 168 s when the ejecta had its cone geometry well-established. The time range of the HST images no longer aligns Dimorphos's location relative to Didymos's with the ejecta cone (Fig. 1a), causing complex ejecta motion near Dimorphos's surface[40]. However, this near-surface ejecta behavior does not affect the cone geometry at the spatial scale of the HST images.

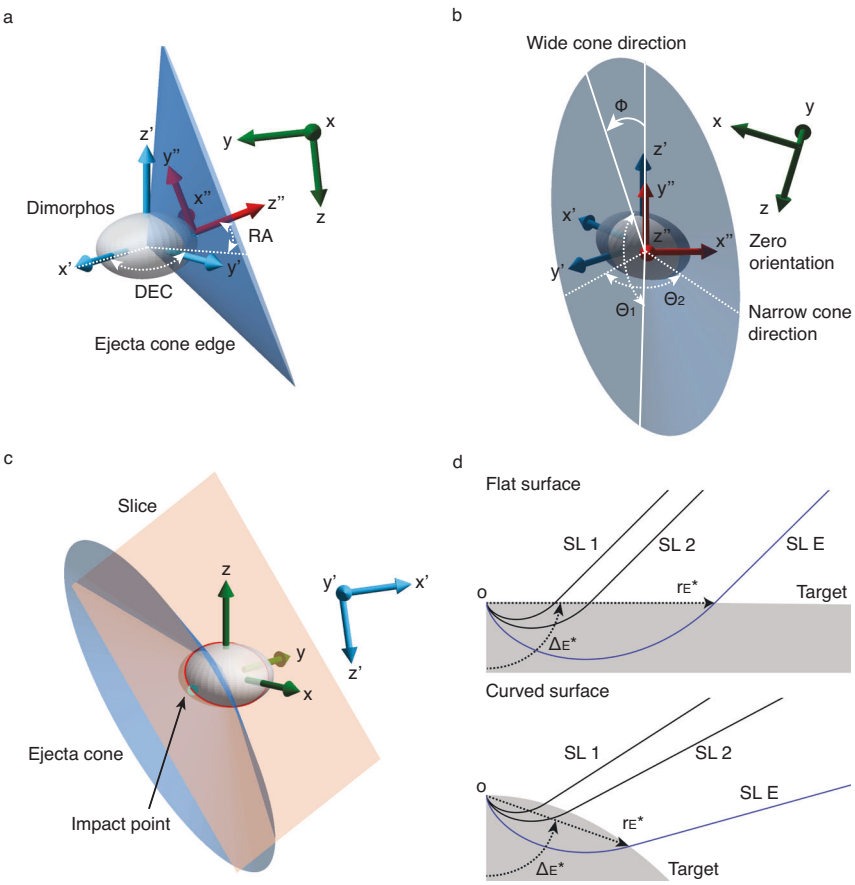

Fig. 1 | Ejecta cone and impact cratering flow fields. The arrows in light blue show (x', y', z') in J2000, while those in green (x, y, z) are the Dimorphos-fixed frame (IAU_DIMORPHOS). The red arrows give the local frame at the impact site. z'' is the DART impact direction, x'' is orthogonal to Dimorphos's north and z'', and y'' is orthogonal to these axes. **a** and **b** Cone geometry and Dimorphos. The cone's perimeter defines its edge. **c** Slice in light red representing a plane used for the Maxwell Z-model. The red curve over Dimorphos represents the intersection between the body and the slicing plane. **d** Illustrations of streamlines defined as *SL*. An example streamtube is a region between *SL*1 and *SL*2. SL E, given in dark blue, is the streamline farthest from the impact site along a given azimuthal piece.

Table 1 | Properties determined by cone measurements and the Maxwell Z-model approach

Quantity	Notation	Value	Units	Frame
Cone geometry	–	–	–	–
Cone wide angle	θ_1	133 ± 9	deg	[–]
Cone narrow-angle	θ_2	95 ± 6	deg	[–]
Axis rotation	ϕ	28 ± 17	deg	Local
Axis right ascension	*RA*	141 ± 4	deg	J2000
Axis declination	*DEC*	20 ± 8	deg	J2000
Apex location, *x*-axis	*x*	− 4 ± 6	m	IAU_DIMORPHOS
Apex location, *y*-axis	*y*	− 3 ± 9	m	IAU_DIMORPHOS
Apex location, *z*-axis	*z*	9 ± 10	m	IAU_DIMORPHOS
Maxwell Z-model	–	–	–	–
Streamtube, shape	*Z*	2.9 ± 0.4	[–]	[–]
Streamtube, speed	α	$(3.1 \pm 2.2) \times 10^{-4}$	$hm^{(Z+1)}/s$	[–]
Streamtube, momentum	γ	0.73 ± 0.12	[–]	[–]
Geometric factor	P_{fl}	44 ± 10	%	[–]

The errors in Value represent 1σ uncertainties. The coordinate frame is J2000, the Dimorphos fixed frame (IAU_DIMORPHOS), or the local coordinate frame (Fig. 1b). For the units, $hm^{(Z+1)}/s$, hm stands for hectometers = 100 m, following the earlier notational definition[65].

Monte Carlo simulations determine the geometry of the elliptical cone (see "Methods", Subsection Ejecta Cone Geometry). Constraints are the position angles (eastward angles from the sky north in J2000) of the cone edges, i.e., the perimeters of the cone seen by both HST and LICIACube. The solution for the cone edge geometry is $\theta_1 = 133 \pm 9°$, $\theta_2 = 95 \pm 6°$, $\phi = 28 \pm 17°$, $RA = 141 \pm 4°$, and $DEC = +20 \pm 8°$ (Table 1). Both narrow- and wide-cone opening angles are wider than an ideal 90° opening angle of an ejecta plume on flat surfaces[48]. The determined azimuthal angle for rotation, $\phi = 28 \pm 17°$, suggests the cone's wide-cone opening direction is preferentially parallel to Dimorphos's north-south direction. Illumination alignments between the cone edges and the terminator on Dimorphos at T + 175 s and T + 178 s constrain the location of the ejecta cone's tip (apex) as $(x, y, z) = (-4 \pm 6, -3 \pm 9, 9 \pm 10)$ m in the Dimorphos body-fixed frame (later known as IAU_DIMORPHOS), in which *x* is toward Didymos, *z* is Dimorphos's north, and *y* is orthogonal to these axes (Fig. 1) (see "Methods", Subsection Ejecta Cone Geometry).

Figure 2 shows the derived cone geometry consistent with that observed by HST and LICIACube. HST images capture the ejecta features extending celestial north and southeast at T + 18,147 s (= T + 5.0 h). LICIACube, on the other hand, observed Dimorphos from different views throughout its CA, which was T + 168 s[41,42]. At T + 160 s, the CubeSat faced the approach side on which the ejecta plume was opening. The spacecraft rapidly approaches the cone and passes at T + 162 s. At T + 170 s, it looks at one side of the ejecta cone. At T + 195 s, the spacecraft observes the entire departure side, mainly looking at the ejecta cone. The angle between the ejecta cone axis and the DART anti-incident direction is 15 ± 5°.

Momentum transfer

How Dimorphos's global curvature contributes to DART's momentum transfer is quantified using the geometric factor, the ratio of the ejecta momentum on a curved surface target to that on a flat surface, P_{fl} (see "Methods", Subsection Geometric Factor). Monte Carlo simulations apply the Maxwell Z-model, an empirical, first-order approximation model, to determine the kinematics of subsurface flow fields and ejecta's ballistic trajectories (see "Methods", Subsection Maxwell Z-model). A material flow follows a single curved trajectory called a streamline, which is a function of the counterclockwise angle from the impact incident direction, Δ, and two kinematic parameters, α and *Z*, representing ejecta's speed and geometry, respectively. A streamtube is a spatial envelope sandwiched by two streamlines. Materials ejected at speeds less than the Dimorphos escape speed (about 9 cm/s) do not influence momentum transfer and are eliminated from consideration. This condition defines the farthest contribution of material excavation, giving the streamline-surface intersection from the impact site, r_E^*, and the resulting angle from the incident direction, Δ_E^* (Fig. 1d). Figure 1d illustrates how a streamtube enclosed by two streamlines, *SL*1 and *SL*2, changes its trajectory and the ejection direction due to surface curvature.

The algorithm uses the measured β[46] as a constraint to determine the geometric factor. The terminal velocities at the surface points of streamtubes give a set of ballistic locations of ejected surface elements at T + 175 s. Comparing these ballistic trajectories with the measured ejecta cone geometry in all azimuthal directions uniquely determines α and *Z*. The method then finds a positive scalar, γ, to make the simulated β consistent with the measured one and determine P_{fl} (see "Methods", Subsection Geometric Factor for DART). Comparison tests confirm the consistency between our approach and the iSALE-2D shock-physics code[49–52] (see "Methods", Subsection Geometric Factor Validation). Monte Carlo simulations, accounting for the above simulation steps, input the cone geometry measurements (θ_1, θ_2, *RA*, *DEC*, ϕ) to give the statistical behaviors of *Z*, α, γ, and P_{fl} (Table 1 and Fig. 3). The results show $Z = 2.9 \pm 0.4$ (Fig. 3a), $\alpha = (3.1 \pm 2.2) \times 10^{-4}$ $hm^{(Z+1)}/s$ (Table 1), where hm are hectometers (= 100 m). Because *Z* inversely correlates with α, *Z* becomes low (high) when α is high (low) (Fig. 3a, b). Lower (higher) *Z* distributions characterized by the extrema cause shallow (steep) ejection.

The ejecta cone, determined from observational data, opened widely at azimuthal angles (ϕ) of about 0° (Dimorphos north) and about ± 180° (Dimorphos south), indicating that the cone extends along almost the Dimorphos north-south direction (Fig. 3c). The slight shift toward a positive azimuthal angle indicates the wide-cone opening direction's slight twist toward the east-west direction, $\phi = 28 \pm 17°$. The range of material excavation derived by the Monte Carlo approach using the Maxwell Z-model, on the other hand, becomes longer in the east-west direction but shorter in the north-south direction. This is because the flow field extent in the north-south direction is limited by Dimorphos's higher curvature in this direction than in the east-west direction. This result contrasts with earlier numerical work suggesting surface curvature might not contribute significantly to the ellipticity of an impact crater[53], mainly because of Dimorphos's high curvature in the north-south direction.

https://doi.org/10.1038/s41467-025-56010-w

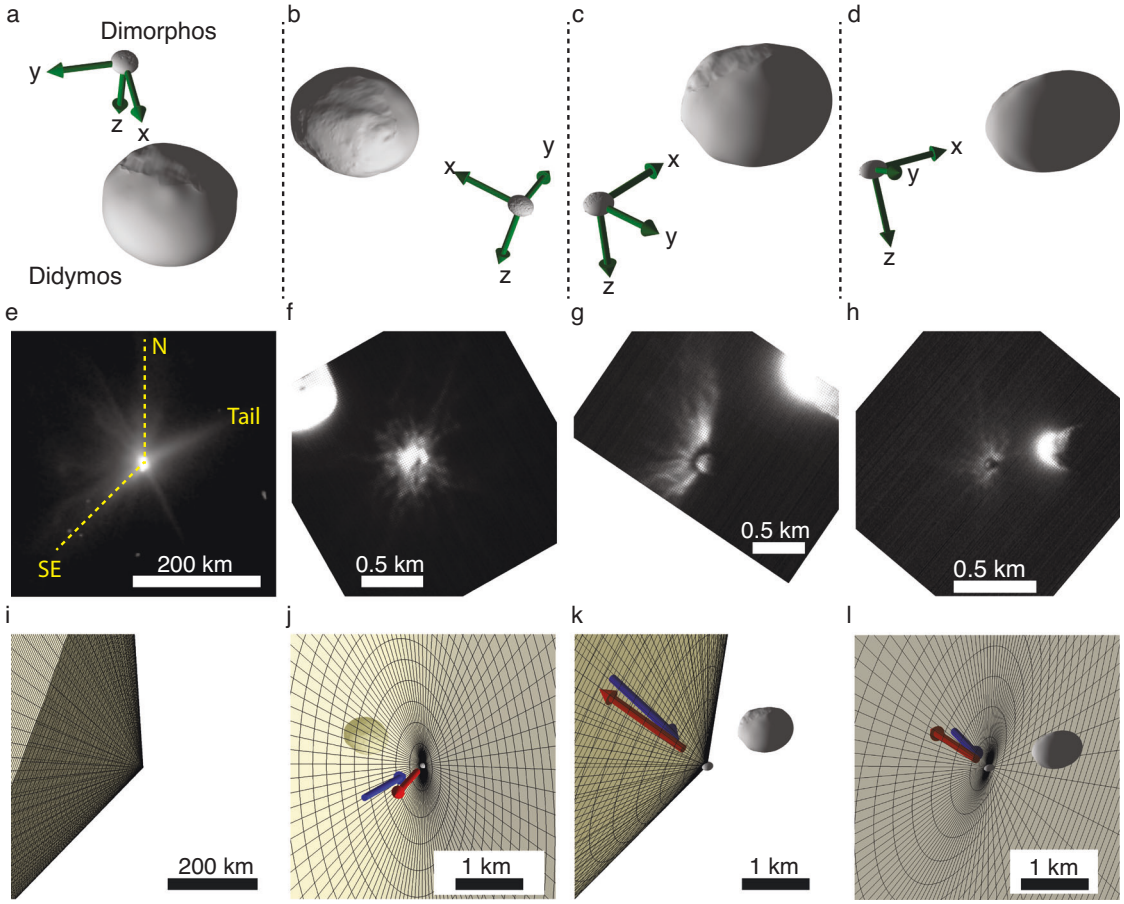

Fig. 2 | Observed and simulated ejecta cone edge geometries. a–d Didymos-Dimorphos orientations seen from observers in J2000. The versions of the Didymos and Dimorphos shape models are Didyv003[96] and Dimov004[30]. The green arrows give IAU_DIMORPHOS as a reference. **e–h** Images taken by observers (HST in **e** and LICIACube in **f–h**). The HST image captures the global structure of the ejecta cone, evolving toward the north (N) and southeast (SE), and the tail extended toward the northwest. All images are centered at Dimorphos. **i–l** Simulated cone geometry in light yellow seen from observers (HST in **i** and LICIACube in **j–l**). The ejecta cone, illustrated as a yellow cone with frames in black, exhibits its geometry differently in HST and LICIACube images. The cone observed by HST (**i**) does not change over the considered time, while that by LICIACube changes dynamically. LICIACube first sees the front side of the cone (**j**), where Dimorphos is hidden behind it. Once passing through it, the spacecraft observes its backside behind Dimorphos (**k** and **l**). The red arrows show the direction of the cone axis, while the blue ones represent the DART incidence angle. Column (**a**, **e**, **i**) shows HST measurement at T + 18,147 s = T + 5.0 h. Columns (**b**, **f**, **j**), (**c**, **g**, **k**), and (**d**, **h**, **l**) give LICIACube measurements at T + 160 s, T + 170 s, and T + 195 s, respectively.

Comparable to the crater radius, half the crater's rim-to-rim distance[48], the average distance of material excavation from the cone axis, i.e., $r_E^* \sin(\Delta_E^*)$, is 54 ± 9 m. This result is larger than the numerically predicted size, which depends on the target's strength. Modeling the DART impact on Dimorphos as a cohesionless target (< 50 Pa) no longer causes a crater-like morphology but generates flatter depression at a radius of 25–55 m[54,55]. The predicted ejecta mass suggests Dimorphos as a weak target (Ferrari et al. in review[56]). If low-moderate material strength (about 1–10 kPa) influenced the impact, it would create a crater 15–30 m in radius (Stickle et al., in review[57]). The derived larger value (54 ± 9 m) may come from our assumption that the cone edge is linear, while its geometry is likely complex and curved around near the impact site, allowing smaller crater excavation to generate a larger ejecta cone[54]. This complexity, culminated by model simplification and uncertainties, causes challenges in inferring the crater size and the target's strength.

The geometric factor relative to a flat surface target in a given azimuthal direction becomes lower but more variable along the wide cone direction (Fig. 3d). The east-west direction (ϕ of about ± 90°) tends to have higher geometric factors with lower uncertainties. This direction offers a flatter surface, providing positive momentum transfer and, thus, positive geometric factors. On the other hand, because of high curvature approximately along the north-south direction (ϕ of about 0° and ± 180°), ejected materials tend to depart toward Dimorphos's anti-along track direction. The Dimorphos-south direction (ϕ of about ± 180°) tends to have negative geometric factors, indicating ejecta's contribution to negative momentum transfer. Again, the ejecta cone's twist causes the shift of lower geometric factors towards positive azimuthal angles by about 45°. The net geometric factor relative to a flat surface target, P_{fl}, is 44 ± 10% for Dimorphos. If the target surface is perfectly flat, the derived geometric factor leads to $\beta = 7.2 \pm 3.8 (1\sigma)$, likely the upper end of the predicted range[11,58].

Discussion

DART-driven impact ejecta cone geometry

While the elliptical cone geometry likely results from many factors, Dimorphos's high curvature in its north-south direction is the major contributor. At the time of impact, DART's solar panels faced the Dimorphos north-south direction at azimuthal angles of $\phi = -2°, 178°$[28], and the spacecraft geometry likely created an elliptical crater excavation, causing complex ejecta cone geometry[8]. Also, these solar panels hit two approximately-six-meter-sized boulders at the impact site, Bodhran (ϕ of about 0°) and Atabaque (ϕ of about 145°)[28].

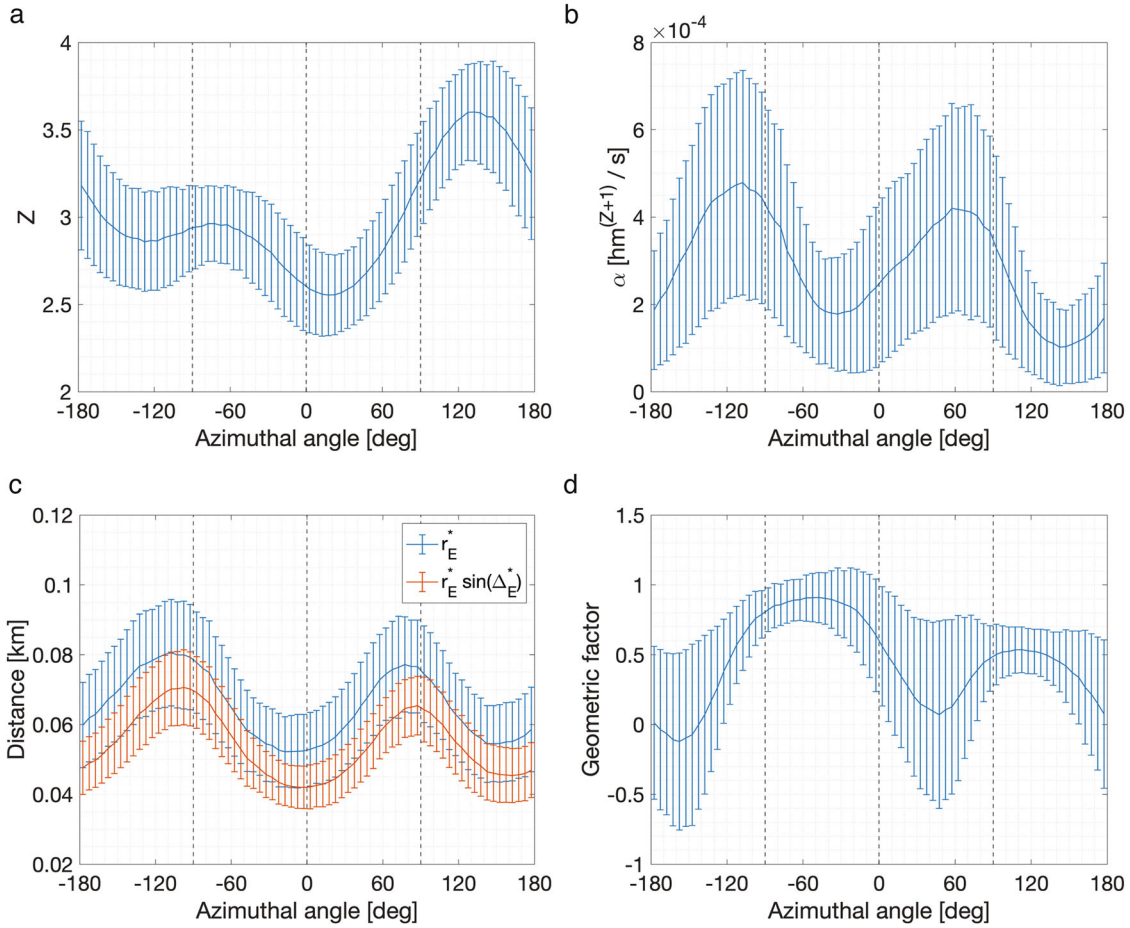

Fig. 3 | Variations provided with error bars in Maxwell Z-model parameters and projected cone geometry onto Dimorphos's surface with azimuthal angle from Dimorphos's north. a Variations in Z. **b** Variations in α. **c** Variations in excavation range from the impact point, r_E^*, in blue, while those from the cone axis, $r_E^* \sin \Delta_E^*$, in red. **d** Variations in geometric factor along each piece in an azimuthal direction. Uncertainties are provided in 1σ by computing the standard deviations of the whole samples per azimuthal angle bin. Source data are provided as a Source Data file.

Recent work suggests that the ejection angle would become shallow in the direction where a boulder exists[59,60]. However, given that the ejecta cone encloses almost half of Dimorphos's body at T + 175 s, the crater likely grows large enough that the contribution of the spacecraft's geometry to the ejecta evolution is no longer significant[54]. Earlier experimental work suggested the crater growth recovers the ejection steepness when the excavation extent exceeds the boulder size[59]. Because the excavation range is tens of meters (Fig. 3c) at this time, the influence on the ejecta cone geometry of both the spacecraft's solar panels (each <10 m) and the pre-existing meter-sized boulders is minimal. Given the elliptical cone, the ejecta plume does not directly cross Didymos, in contrast to the earlier suggestion that the ejecta might directly hit the asteroid based on the circular ejecta cone assumption[42].

The fact that the measured wide-cone dimension twists toward the east-west direction by $28 \pm 17°$ is still under investigation. With increasing curvature, an ejecta plume becomes shallower relative to the initial surface[20], so the wide-cone opening dimension should be ideally parallel to the Dimorphos north-south direction. While no decisive explanation exists, this twist may relate to the complex ejecta morphology. The observed ejecta morphology is highly heterogeneous[41,42,61], including complex ray structures, clump and boulder distributions, and hole-like features lacking materials. Small particles and boulders interact in the ejecta cone, flowing around them like obstacles, leading to directional inhomogeneities in the ejecta plume. The interactions between small particles and larger boulders complicate the ejecta plume structure[62]. Boulders at various speeds[33,61] would change the ejecta plume structure with time. Such interactions within the ejecta plume, which may be attributed to structural heterogeneity in Dimorphos[19], might be responsible for deviations in the ejecta cone geometry from the ideal cone geometry. The DART impact with slight obliquity (i.e., the 73° impact angle) likely does not influence the ejecta cone geometry much, given recent experimental work showing that oblique impacts with an impact angle of higher than 60° exhibits symmetric cone geometry over the azimuthal direction[63]. Regardless of the wide cone's slightly twisted orientation, its preferred orientation toward the Dimorphos north-south direction does not change.

Geometric factor on Dimorphos

The derived geometric factor, $P_{fl} = 44 \pm 10\%$, suggests that the contribution of ejecta momentum to momentum transfer decreases by a factor of larger than two compared to the same impact on a flat surface. This low geometric factor results from Dimorphos's higher curvature in its north-south direction. Based on the asteroid's pre-impact extents, the ratio of the semi-minor axis (c) to the semi-major axis (a) is 0.64[30]. Because Dimorphos's higher curvature in its north-south direction causes a shorter excavation range, the flow fields beneath the surface are short-lived. Therefore, excavated materials cannot change their flow directions well enough to achieve a higher ejection angle from the surface before launch. Such trends are so extreme in some directions that ejecta momenta possess anti-along track components, giving negative momentum transfer (Fig. 3d). These mechanisms noticeably reduce the net momentum transfer. The observed clumps and boulders ejected from Dimorphos may also contribute to the off-track

momentum transfer but not significantly to the along-track component[61]. If the DART impact-driven crater were small relative to Dimorphos's size, local morphological features would be more influential than global curvature. Deep Impact and SCI represent small impact conditions relative to the target size.

Given its limited settings, our Maxwell Z-model approach only gives first-order approximations of the flow fields. However, it offers insights into the DART impact on Dimorphos's curved surface. The variations in Z over different azimuthal angles, i.e., $Z = 2.9 \pm 0.4$, are similar to those observed for a flat surface[63–65], and its mean is consistent with the model's ideal case, i.e., $Z = 3$[48]. This finding indicates that regardless of Dimorphos's high curvature, the typical value of Z for a flat surface target can reproduce the momentum transfer with a new scalar parameter, γ. One caveat is that the model parameters are set to be constant throughout the ejecta evolution. Earlier reports suggest Z increases with Δ[66]. Z is approximately 2 when Δ is about 0°, meaning non-rotational flows, while $Z \geq 4$ when $\Delta \geq 75°$. Thus, when Δ is high, flow rotation also becomes high, giving a higher ejection angle from the surface horizon.

Geometric factors on near-earth Objects less than 50 m radius

The low geometry factor of the DART impact due to Dimorphos's north-south high curvature suggests necessary considerations of a target's curvature to predict kinetic deflection accurately. When the crater size is large relative to a target's size, a more practical case due to a typical desire for higher kinetic deflection, global curvature influences the flow fields and, thus, the cone geometry. The geometric factor decreases if the curvature is high, leading to a lower momentum transfer. Applying our Maxwell Z-model approach enables quantifying how the geometric factors change due to the impact locations for 99 NEOs less than 50 m in radius observed by the MANOS (Mission Accessible Near-Earth Objects Survey) project[67,68]. The reason for focusing on objects less than 50 m in radius comes from recommendations from publicly available reports[1–4]. Limited observation constraints add an assumption to the present study that each NEO sample is a prolate body with identical semi-intermediate and semi-minor axes (see "Methods", Subsections Light curve samples from MANOS and Geometric factors for MANOS samples). Each body is set to have two impact locations: one along the semi-major axis and the other along the semi-minor axis. Because the impacts at both locations are vertical with respect to the local surface, the impact point along the semi-major axis has higher curvature.

Monte Carlo simulations, using the established Maxwell Z-model combined with the π-scaling relationship[24,69,70] (see "Methods", Subsection Transient Crater Radius), determine the statistical trends of the geometric factors of all samples (see "Methods", Subsection Geometric Factor for MAMOS Data). Impactors are assumed to have the same impact energy as DART. The analysis concept is to apply the derived Maxwell Z-model parameters from the DART study while α is independently determined for each sample. One key parameter for the α computation is the strength of each sample. While the strength is unknown, their spin states may constrain their lower bound. Some NEOs spin exceptionally rapidly, while others do not. Depending on their spin states, some objects should have mechanical strengths to stay structurally intact[71]. A semi-analytical stress analysis computes the minimum cohesive strength for each body to keep the structure intact, which is used for the α computation (see "Methods", Subsection Minimum Cohesive Strength).

Figure 4 shows the distributions of the geometric factors of the samples. The geometric factor positively correlates with the target radius and strength (Fig. 4a, b). Given a constant impact energy identical to the DART impact, higher strength, and a larger target radius make the transient crater radius small relative to the body[69], reducing the curvature effect and thus making the geometric factors higher. The transition zone from zero geometric factors (= 0%) to high geometric factors (>70%) is narrow. This zone also overlaps the predicted catastrophic disruption threshold, which defines an impact condition when the final target mass is less than half the original (see "Methods", Subsection Catastrophic Disruption Threshold). However, this predicted range is generally broad, given the higher uncertainties of models and parameters. The standard deviation increases when the geometric factor decreases because the uncertainty is more sensitive to the variations in the empirical parameters when an impact affects a larger volume in a target.

Figure 4c and d show the distribution of the relative geometric factor, defined as the difference between an impact along the semi-major axis and an impact along the semi-minor axis. The results show lower relative geometric factors along the semi-major axis than the semi-minor axis for all samples. This is because impacts along the semi-major axis encounter higher curvatures. The variation of a relative geometric factor with strength and radius appears more random, indicating the geometric factor's dependence on the curvature. This finding suggests the importance of a target's curvature for kinetic deflection. Therefore, selecting a flatter impact point on the target is crucial to enhancing momentum transfer.

Kinetic deflection strategy learned from DART

The increase in the encounter speed is reported to make such single impacts with high kinetic energy more feasible[72]. Another concept may be to disrupt a target body as part of kinetic deflection[73]. However, our finding suggests that scenarios employing a single impactor having higher kinetic energy are not ideal because the efficiency of momentum transfer changes due to global curvature (Fig. 5). A flatter surface target offers higher momentum transfer for a single impact with a given kinetic energy due to higher changes in the subsurface flow fields. Alternatively, a lower kinetic energy impactor results in a smaller crater that is less affected by global curvature, increasing momentum transfer efficiency. With these trends to enhance momentum transfer, employing multiple, smaller impactors is a better solution than having a single, large impactor. In the multiple-impactor scenario, each impactor has a smaller kinetic energy than one in the single-impactor scenario. Still, the net kinetic energy can be comparable when all impactors collide with the target. Practically, the multiple-impactor scenario can send impactors at different times and aim at flatter surface points on the target, maximizing the net momentum transfer (Fig. 5). However, the crater size should not be too small because local boulders and topography can become more influential on the ejecta plume formation, as seen by earlier experimental tests[62], changing the trends of momentum transfer. This condition applies to Deep Impact and Hayabusa2, which observed complex ejecta formation[22,26].

Constraining the physical properties of a target object before kinetic impact is essential. While no details have been reported for global curvature[4] in the past, this study proposes it as a key contributor that can easily change the efficiency by a factor of a few. The practical approach is to visit the object in situ and conduct key measurements as much as possible before deciding the timing of kinetic deflection. A rapid response to this demand after identifying a potential threat is not yet a mature technology[4]. Compared to mass measurement, which requires additional operational constraints, imaging the target even during a fast flyby can provide sufficient information to infer the curvature and surface conditions, significantly improving the accuracy of momentum transfer. The proposed multi-impactor scenario can also offer additional reconnaissance before the planned collisions at different times. Such multiple observations enable tracking possible large-scale modifications that a target may have altered early impacts. Global shape deformation is one of such modifications. Dimorphos likely changed its shape significantly due to the DART impact[74,75], experiencing additional orbital perturbation[70,76,77]. Demonstrating capabilities to acquire such properties by a rapid reconnaissance mission is strategic to achieving sophisticated advances in kinetic deflection technologies[78].

https://doi.org/10.1038/s41467-025-56010-w

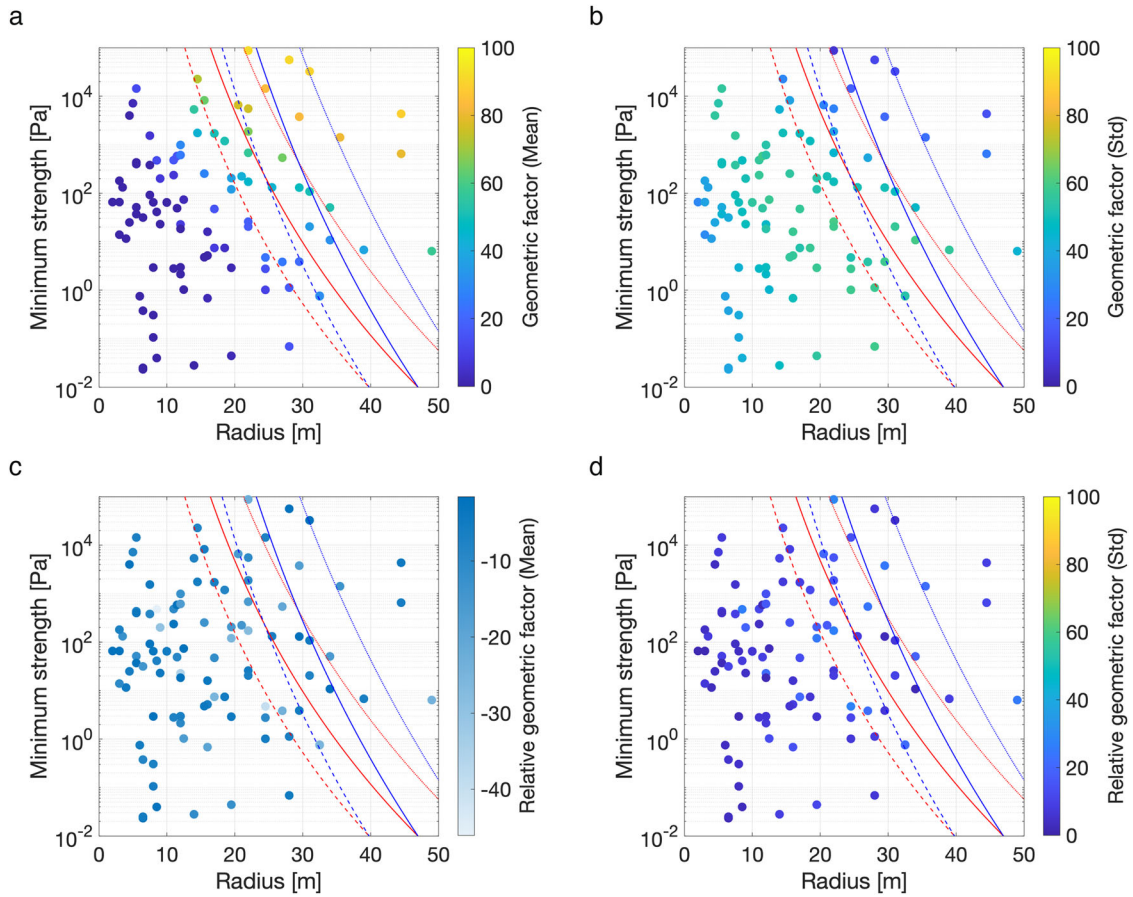

Fig. 4 | Geometric factor distributions of 99 small NEOs measured by the MANOS project[67,68]. **a** and **b** Mean and standard deviation of the geometric factor for an impact along each target's semi-minor axis. **c** and **d** Mean and standard deviation of the relative geometric factor of an impact along the semi-major axis to one along the semi-minor axis. All panels give the geometric factor distributions in percentile as a function of diameter and minimum strength. All negative outcomes in Panels (**a** and **b**) are truncated and noted as zero geometric factors. The curves in different colors, calculated using Equation (23), show interpolations between the catastrophic disruption thresholds for a pumice-like target and a cohesionless target (red) and a basalt-like target and a cohesionless target (blue). For the cohesionless target, we assume a minimal strength of 0.01 Pa. The dashed, solid, and dotted lines give bulk densities of 1000 kg/m^3, 2000 kg/m^3, and 4000 kg/m^3. If target asteroids stay on the right side of those thresholds, they do not experience catastrophic disruption. Source data are provided as a Source Data file.

Methods

Ejecta cone geometry

Similar to earlier work[40,46], the present measurements apply J2000 to describe the cone axis direction. In this subsection, "north" and "south" mean the celestial north and south, respectively. The ejecta projected onto the view plane of HST and LICIACube images (Table 2) gives the position angles of the cone edges. For each image, the maximum counts of bright pixels identify the directions of the linear features. Images are categorized as the side view if obvious bright features exist; otherwise, they are sorted out as the front view for earlier time stamps or the back view for later time stamps. HST images only show the cone's side view[40], while LICIACube images change the view with time[47]. The sorting process of LICIACube images intentionally accounts for the front and back sides because they narrow the range of the cone orientation. The dynamical states of the asteroids and spacecraft come from the DART mission-driven SPICE kernels with a version of d430. The resulting impact angle (from the local horizon) is 73°[28].

Five LICIACube images taken at 160–195 s after the DART impact (T + 160–195 s) capture the ejecta plume at speeds of about 20 m/s. These images also enable measuring Dimorphos's center of the figure, compared with the simulated rim locations generated by the Dimorphos shape model. Six HST images taken at T + 0.41–8.2 h[40] offer the ejecta geometry consisting of ejected particles with comparable speed to those observed by LICIACube. Removing multiple sources unrelated to the cone edges, including diffraction spikes and a tail that evolved due to solar radiation pressure[40], effectively determines the position angles of the cone edges.

The position angle search obtains the position angle at the bright-pixel count's peak as a mean and the peak's width as a 1σ uncertainty (Table 2). Finding the width is not challenging because the peak is a single set with a Gaussian-like distribution without overlapping with other peaks. Averaging out the measurements of all HST images reduces the number of data samples to a single sample, as HST's view plane does not change significantly. For LICIACube images, the samples at the earliest and latest epochs capture the front and back sides of the ejecta cone.

The cone geometry determination process uses the measured position angles to obtain the cone's geometric parameters ($DEC, RA, \phi, \theta_1, \theta_2$), assuming the ejecta cone geometry is time-invariant. The following formula gives the score for the k-th image:

$$X_k = \sum_{i=1}^{2}\sum_{j=1}^{n} \frac{1}{\sqrt{2}\sigma_{k,i}} \exp\left\{-\frac{(x_{k,j}-\mu_{k,i})^2}{2\sigma_{k,i}^2}\right\} \quad (1)$$

where n is the number of pixels in the image, and i represents the northern and southern edges. $x_{k,j}$ is the position angle of a simulated pixel j, $\mu_{k,i}$ is the mean of the measured northern or southern edges, and $\sigma_{k,i}$ is its standard deviation. The final score is a sum of

https://doi.org/10.1038/s41467-025-56010-w

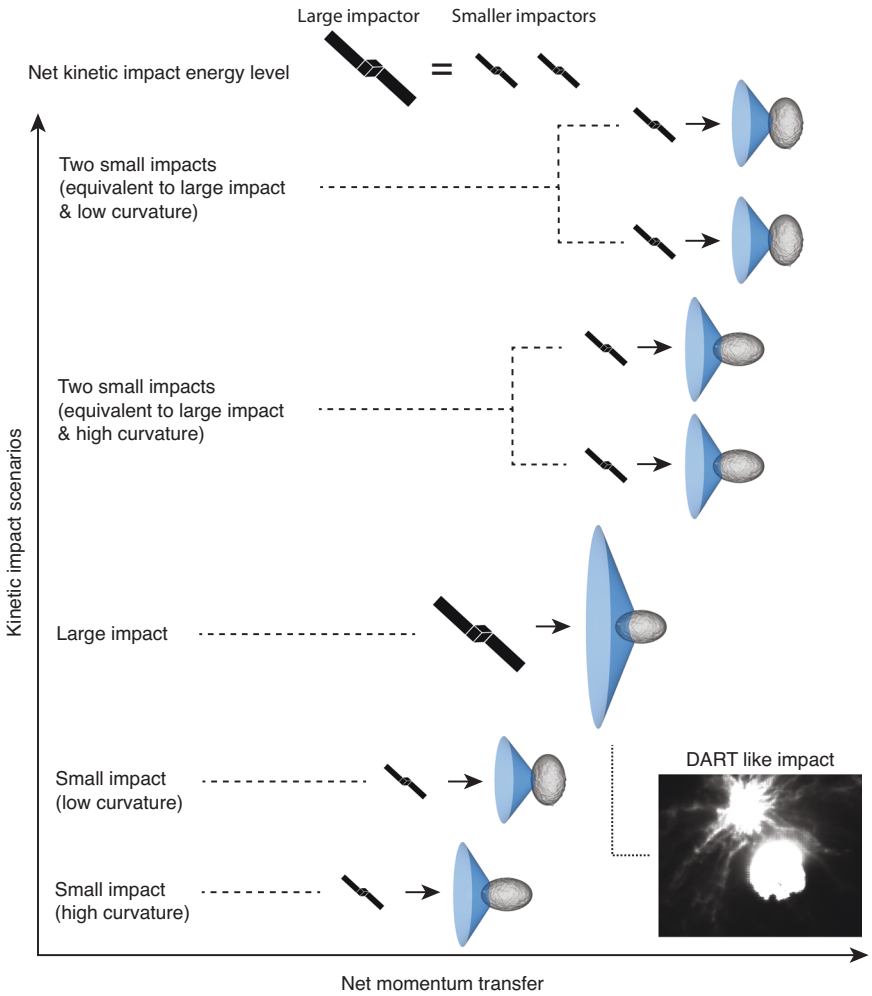

Fig. 5 | Schematics for kinetic impact-driven momentum transfer depending on different scenarios. Impactors with two kinetic energies add the same net kinetic energy to a target by performing multiple impacts. Net momentum transfer changes due to orientation and kinetic energy per impactor. A larger impactor may add higher kinetic energy at once, possibly causing the resulting ejecta cone to be affected by an asteroid's curvature and have a lower kinetic deflection efficiency. Multiple smaller impactors hitting lower-curvature sides of targets may increase a net kinetic deflection efficiency. The ID of the attached LICIACube image is liciacube_luke_l0_1664234219_00112_01.fits.

Table 2 | Position angle measurements using LICIACube LUKE and Hubble Space Telescope (HST) images used in the present analysis

Obs Frame	HST Orbit ID	UTC	Exposure	Time + I	North	South
HST	01	09-26T23:39:00	25	1476	4.3 ± 8	130.7 ± 8
HST	02	09-27T01:06:22	25	6718	–	–
HST	03	09-27T02:45:34	50	12,700	–	–
HST	04	09-27T04:16:51	25	18,147	–	–
HST	05	09-27T05:52:07	25	23,863	–	–
HST	06	09-27T07:27:22	25	29,578	–	–
Obs Frame	**LICIACube Image ID**	**UTC**	**Exposure**	**Time + I**	**North**	**South**
LCC1	1664234224	09-26T23:17:04	30×10^{-3}	160	[–]	[–]
LCC2	1664234239	09-26T23:17:19	30×10^{-3}	170	−10.0 ± 5	146.0 ± 5
LCC3	1664234242	09-26T23:17:22	30×10^{-3}	178	−17.0 ± 5	152.0 ± 5
LCC4	1664234247	09-26T23:17:27	30×10^{-3}	183	−33.0 ± 20	158.0 ± 20
LCC5	1664234259	09-26T23:17:39	30×10^{-3}	195	[–]	[–]

Obs is the observer, either LICIACube or HST. The Coordinated Universal Time (UTC) uses a format of [MM-DDThh:mm:ss]. Time+I and Exposure give the time after the impact and the exposure time in seconds. As a reference, the time of impact is 09-26T23:14:24[28]. Columns North and South show the position angles of the northern and southern cone edges in degrees in J2000. The frame defines the data samples used in the analysis. The position angles measured using HST images display averaged values over all orbit IDs.

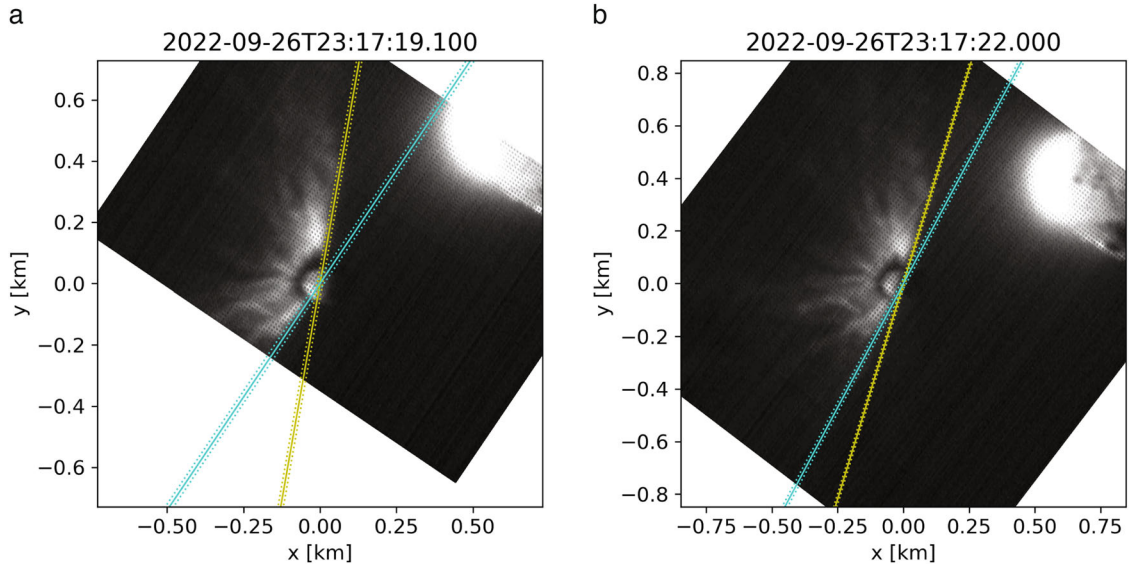

Fig. 6 | Cone edge alignments determined using LICIACube images. a 09-26T23:17:19 (LCC2). **b** 09-26T23:17:22 (LCC3). Table 2 defines Frame IDs. The cyan lines illustrate the alignments of the southern ejecta cone edge, while the yellow lines define the northern cone edge. The solid line is the mean alignment, while the dashed lines give cone edge variations, which defined 1σ uncertainties in this work. Both panels show the cone orientation in J2000. Source data are provided as a Source Data file.

$X_k (k = 1, \ldots, 6)$. The score of the k-th image becomes zero if the view conditions are inconsistent in the simulated and measured cone geometries. For example, such a condition includes when the simulated cone geometry predicts either front or back views while the measured cone is in the side view. Monte Carlo simulations consider 500 cases by varying the measured position angles based on Gaussian uncertainties.

Determining the location of the cone apex uses two LICIACube images, LCC 2 and LCC 3, as they offer the side view of the ejecta cone and Dimorphos's shape, partially illuminated by the sun. Extraction of the alignments between the ejecta cone edge regenerated by the measured geometric parameters and the terminator on Dimorphos (Fig. 6) identifies the cone apex location with 1σ uncertainties. One issue is that using LCC2 and LCC3 does not sufficiently constrain the apex location along the out-of-plane direction uniquely. To avoid this issue, the cone apex determination assumes the cone axis crosses the DART impact site as closely as possible. Monte Carlo simulations account for 30,000 cases by parameterizing the measured cone's geometric parameters (Table 1) to determine the case where the cone axis is the closest to the DART impact site. Simulations are rejected if the simulated cone edge is outside the 1σ uncertainties of the measured alignments. 1000 sets of this routine give the apex location in IAU_DIMORPHOS as $(-4 \pm 6, -3 \pm 9, 9 \pm 10)$ m.

Maxwell Z-model

The basic version of the Maxwell Z-model consists of three kinematic equations[79]:

$$r = r_0 (1 - \cos\Delta)^{\frac{1}{Z-2}} \tag{2}$$

$$v_r = \frac{\alpha}{r^Z} \tag{3}$$

$$v_\Delta = v_r (Z - 2) \frac{\sin\Delta}{1 + \cos\Delta} \tag{4}$$

where r is a mass element's radial location along a streamline, while v_r and v_Δ are its radial and tangential speeds, respectively. These quantities vary with Δ, a counterclockwise angle from the impact incident direction (Fig. 1). For a vertical impact on a flat surface, the downward direction is $\Delta = 0°$. r_0, α, and Z represent a streamline's kinematics. r_0 controls the size of the streamline, Z defines how sharply the streamline changes its direction, and α gives a material ejection speed. Among the kinematic parameters, α also correlates with gravitational acceleration, g, and the transient crater radius, R, which can be determined using the π-scaling relationship[80]:

$$\alpha = \left\{ \frac{g R^{2Z+1}}{4Z(Z-2)} \right\}^{\frac{1}{2}} \tag{5}$$

Computation of transient crater radius

The π-scaling relationship provides the transient crater volume, V[69]:

$$V = K_1 \left(\frac{m_i}{\rho_t} \right) \left\{ \left(\frac{g r_i}{v_i^2} \right) \left(\frac{\rho_t}{\rho_i} \right)^{-\frac{1}{3}} + \left(\frac{Y}{\rho_t v_i^2} \right)^{\frac{2+\mu}{2}} \right\}^{-\frac{3\mu}{2+\mu}}. \tag{6}$$

where K_1, μ, and Y are empirically determined parameters. m_i, r_i, and v_i are the impactor's mass, radius, and speed, respectively. The used values for the parameters are provided in Supplementary Table 1. Y is the strength parameter. ρ_t and ρ_i are the bulk densities of a target and an impactor, respectively. The following equation then provides the transient crater radius using the transient crater volume:

$$R = \left(\frac{3V}{\pi} \right)^{\frac{1}{3}} \tag{7}$$

This parameter is hypothetical in this study, given that it is usually defined for an impact on a flat surface[69] and should be larger than the excavation range, r_E^*.

Computation of minimum cohesive strength

Equation (6) needs the strength parameter, Y, as an input to determine the transient crater volume in Equation (7). This study assumes that this strength parameter is comparable to the minimum cohesive strength, i.e., the lowest cohesive strength that keeps the original object structurally intact. This assumption leads to an upper bound of the crater

size derived by the π-scaling relationship (see "Methods", Subsection Transient Crater Radius). Semi-analytical framework[81,82] computes the minimum cohesive strength using a target's ellipsoidal shape, bulk density, and spin state. Linear elasticity gives a semi-analytical stress field when the body's rotation is in the principal axis mode. This process is independent of Young's modulus. Using the same notation with the strength parameter, Y, for the minimum cohesive strength formulates the following Drucker-Prager yield criterion:

$$Y = \frac{1}{\kappa}(\lambda I_1 + \sqrt{J_2}) \tag{8}$$

$$\lambda = \frac{2\sin\psi}{\sqrt{3}(3-\sin\psi)} \tag{9}$$

$$\kappa = \frac{6\cos\psi}{\sqrt{3}(3-\sin\psi)} \tag{10}$$

where I_1 and J_2 are pressure and shear stress invariants, respectively, and ψ is the angle of friction, which is fixed at $\psi = 35°$[83]. This provides the spatial distribution of the minimum cohesive strength over the entire body. The process selects the maximum value of Y over the object, which usually appears at the center at a short spin period[82]. The π-scaling relationship uses this computed Y to determine the transient crater radius, R.

Definition of geometric factor

The geometric factor, P, defines the ratio of the along-track momentum carried by ejecta on a curved surface to that by a vertical impact on a geometrical reference:

$$P = \frac{L_T}{L_{Tref}} = \frac{\beta - 1}{\beta_{ref} - 1} \tag{11}$$

where L_T and L_{Tref} are the along-track ejecta momenta that form on the curved and reference surfaces, respectively. These scalars are also equivalent to the following vector expressions, $L_T = \mathbf{L}\cdot\mathbf{n}_T$, where $\mathbf{L}$ is the ejecta momenta on the curved surface and $\mathbf{n}_T$ is the along-track unit vector, and similarly, $L_{Tref} = \mathbf{L}_{ref}\cdot\mathbf{n}_T$, where $\mathbf{L}_{ref}$ is the ejecta momentum on the reference surface. P can be convertible with β for these targets, where β_{ref} is β for a reference surface. The reference surface can be arbitrary, but the simplest one may be a flat surface, which generally offers the highest ejecta momentum among any convex surface.

Two reference surfaces considered in this work are a flat-surface target for the DART impact on Dimorphos and kinetic impacts on the MAMOS samples and a spherical target for the comparison test using iSALE-2D. The geometric factor for a flat surface target is P_{fl}, while that for a spherical target is P_{sp}. Using a spherical target for the comparison test results from applying well-established and calibrated simulation results from iSALE-2D. On the other hand, using a flat surface, which generally gives the highest efficiency among convex surfaces, can offer simple diagnostics of the momentum transfer efficiency. For example, reading P_{fl}'s unity value can give a direct insight into how close (far) the momentum transfer is to (from) the ideal case. However, P_{sp} does not give such insightful views easily because it can be larger than unity even when the ejecta momentum does not reach the flat surface case.

Light curve samples from MANOS

Samples are available through the MANOS light curve campaigns, which offer samples' spin periods, sizes, and shapes. The project sampled 308 NEOs over 4.5 years[68]. Many samples are smaller targets less than 50 m in radius, unlike those cataloged in the Asteroid Lightcurve Database, which archives larger objects in general[84]. 99 sample objects have full and partial light curve data over their spin periods[68]. Each sample's shape is assumed to be a biaxial ellipsoid, where its semi-intermediate and semi-minor axis are equal. When the semi-major axis is a, and the semi-minor (intermediate) axis is b, this ratio becomes b/a. Using an available relative amplitude, Δm, results in b/a, given the following equation:

$$\Delta m = -2.5\log\left(\frac{b}{a}\right) \tag{12}$$

Geometric factor of DART impact on Dimorphos

Slicing the asteroid's body parallel to the DART incident direction makes thin pieces over all azimuthal directions, each slice later called an azimuthal piece. Each azimuthal piece defines a volume at an azimuthal angle, extending to the normal direction to the DART incident direction, and thus looks like a wedge. While the number of azimuthal pieces is arbitrary, 100 pieces give acceptable computational accuracy without adding significant computational burdens. The Maxwell Z-model approach determines α, Z, and a new scaling parameter controlling the net momentum, denoted as γ. A developed scheme uniquely determines α and Z for each azimuthal piece by comparing the measured cone geometry with the spatial distribution of ejected surface materials in 10,000 streamtubes in each azimuthal piece at 177 s, the mean time of imaging for LCC2 through LCC4.

The determined α and Z for all azimuthal pieces give the ideal momentum, $\mathbf{L}_p$, as the sum of each streamtube's mass times its surface velocity, $dm\mathbf{v}_{\Delta^*}$, where dm is the streamtube's mass and $\mathbf{v}_{\Delta^*}$ is the ejection velocity:

$$\mathbf{L}_p = \sum_{i=1}^{m}\sum_{j=1}^{n} dm_{i,j}\mathbf{v}_{\Delta^* i,j} \tag{13}$$

where i and j are the indices representing an azimuthal piece ($1 \le i \le m$) and a streamtube in one azimuthal piece ($1 \le j \le n$). However, Equation (13) is unrealistic because this does not account for energy loss within each streamtube. For model simplicity, introducing γ yields the actual ejecta-carried momentum:

$$\mathbf{L} = \sum_{i=1}^{m} r_{0,i}^{\gamma}\mathbf{L}_{p,i} \tag{14}$$

where $\mathbf{L}_{p,i}$ and $r_{0,i}$ are the momentum and r_0 of an azimuthal piece of i, and γ takes the same value over the entire azimuthal pieces. The reason for introducing γ as a power of $r_{0,i}$ was to ensure that γ is consistent over the entire azimuthal pieces regardless of the variations in $r_{0,i}$. However, this equation must keep the units on both sides consistent, needing $r_{0,i}^{\gamma}$ to be dimensionless. Considering an alternative form dividing $r_{0,i}$ by its unity length, i.e., $(r_{0,i}/1)^{\gamma}$, can mitigate this issue. This way, $\mathbf{L}$ and $\mathbf{L}_p$ have consistent units.

Given the geometric parameters, cone apex location, β, α, and Z, the algorithm iteratively determines γ such that Equation (15) satisfies under an error threshold for γ of 0.01%. This process first computes the simulated β using its form[6,46]:

$$\beta = 1 + \frac{\mathbf{L}\cdot\mathbf{n}_T}{(\mathbf{E}\cdot\mathbf{L}_{sc})\cdot(\mathbf{E}\cdot\mathbf{n}_T)} \tag{15}$$

where $\mathbf{E}$ is the unit vector of the net ejecta momentum, and $\mathbf{L}_{sc}$ is the momentum carried by the spacecraft. Supplementary Table 2 gives the values of the Dimorphos along-track direction ($\mathbf{n}_T$) and the DART incident direction. The process then uses a Newton method to obtain γ by comparing the simulated β with the measured one[46]:

$$\beta = (3.61 \pm 0.2)\frac{\rho}{\rho_{ref}} - 0.03 \pm 0.02(1\sigma) \tag{16}$$

where ρ_{ref} is the reference bulk density fixed at 2400 kg m^{-3}, and ρ is the considered bulk density, which is 2, 400 ± 900(1σ) kg m^{-3}.

Each Monte Carlo simulation also calculates the ejecta momenta on a reference surface. Computing it uses the same inputs, including the azimuthal variations in α and Z. However, it does not perform the iterative scheme to compute γ but uses the value obtained above. Applying the derived ejecta momenta on both curved and reference surfaces to Equation (11) results in P_{fl}. Running 1000 Monte Carlo simulations with Gaussian-distributed inputs offers the statistical behaviors of P_{fl} (Table 1).

Validation of geometric factor computation by Maxwell Z-model

Comparisons between the Maxwell Z-model and iSALE-2D simulations[49–52] reveal that both models give consistent geometric factors relative to a spherical target (Fig. 7). In this test, nine iSALE-2D simulations with different biaxial ellipsoids offer variations in β, assuming that each target's along-track direction corresponds to an impactor's anti-incident direction. The target dimension is $2a \times 2b \times 2c$, where $b = c$. The simulations parameterized b/a, which ranged between 0.4 and 2.0 with an increment of 0.2. The equivalent radius is 75 m for all cases. To mimic the DART impact condition, each case assumes a low-density impactor modeled as a sphere with a radius of 1.2 m and a mass of 580 kg. The impact speed is 6 km/s, and the impact site is along the axis. We determine β for each case to obtain P_{sp}.

The present iSALE-2D simulations follow the parameter settings from earlier work[10,12]. The impactor's material behavior follows the Tillotson equation of state (EOS)[85] and the Johnson-Cook strength model for aluminum[86]. The target's behavior follows the Tillotson EOS for basalt[87] with a modified grain density of 3500 kg/m^3, which corresponds to the average grain density of L/LL chondrites[88]. The current version of iSALE-2D sets a simple pressure-dependent strength model to define the target's shear strength[50], with a cohesive strength of 1 Pa and a coefficient of internal friction of 0.55. The target's porosity is 45% at the initial condition, and its behavior follows the $\epsilon - \alpha$ compaction model[51]. All parameters are available in Supplementary Table 1. Given impact scaling relationships[89], the iSALE-2D results may recreate impact behaviors given in the range of $Z = 2 - 3$, where Z is the Maxwell Z-model kinematic parameter.

The Maxwell Z-model approach explores the statistical trends of P_{sp} by considering Gaussian-based inputs to the model based on our earlier analysis for Dimorphos ($Z = 2.932 \pm 0.406$ and $\gamma = 0.731 \pm 0.120$) and those from the literature of the π-scaling relationships ($K1 = 0.22 \pm 0.02$ and $\mu = 0.47 \pm 0.07$). These π-scaling parameters assume impacts on dry sands and rocks[24]. The impactor's bulk density, another input parameter in the model, is fixed at constant at 1925 kg/m^3 for all cases to make this test consistent with the iSALE-2D runs. The strength parameter, Y, is set to be 1 Pa to mimic vertical impacts on cohesionless targets. The analysis performs 1200 runs with Gaussian-distributed inputs for each b/a case. Some unrealistic solutions exist, giving extremely high or low P_{sp}. Such solutions come from parameter conditions at the tails of their distributions or simply ill-defined numerical values for the parameter conditions. The post-processing steps remove any solutions being higher than 200% or lower than −200%, removing 15–25% of all solutions, having no significant impact on the statistical trends of our results.

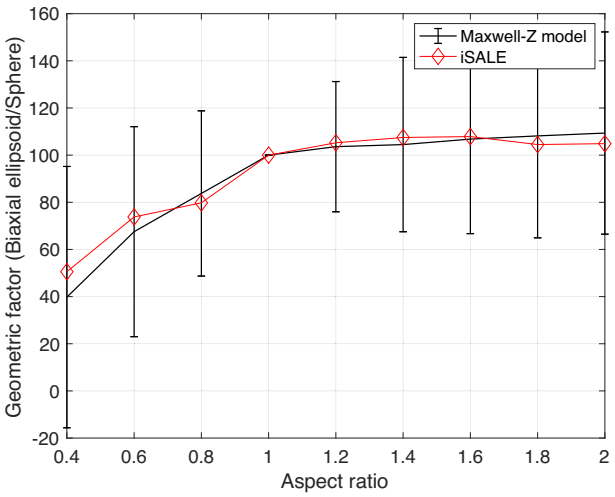

Fig. 7 | Result comparison between Maxwell Z-model and iSALE-2D simulations. The x-axis is the aspect ratio of the biaxial ellipsoid target with dimensions of $2a \times 2b \times 2c$, where $b = c$, and the y-axis is the geometric factor relative to a spherical target, P_{sp}, in percentiles. The aspect ratio is defined as b/a. The black line with error bars resulted from Maxwell Z-model simulations, while the red line was from iSALE-2D simulations. The Maxwell Z-model's error bar gives 1σ uncertainties. Source data are provided as a Source Data file.

Geometric factors for MANOS samples

Simulations for each sample perform two geometric factor computations. The first computation considers an impact along the semi-minor axis, while the second one simulates that along the semi-major axis. All simulations assume vertical impacts with the same impact scale as the DART impact, leading to axisymmetric ejecta momenta. The assumption is that the along-track direction corresponds to an impactor's anti-incident direction. With these simulation settings, impacts along the semi-major axis experience a higher curvature than those along the semi-minor axis. The simulation scheme is the same as the geometric factor computation for the DART impact on Dimorphos, which determines P_{fl}. However, there are two differences. First, this scheme uses the parameters determined from the DART impact case, except for α. Second, α comes from Equation (5) because it depends on R and g, inconsistent with the DART impact case. R is determined using the π-scaling relationship, where Y comes from the minimum cohesive strength. Key inputs in the π-scaling relationship are compiled in Supplementary Table 2.

Monte Carlo simulations give the statistical behavior of each sample's geometric factor. The bulk density in this test ranges between 1000 and 4000 kg/m^3 to cover its uncertainties. This distribution varies Y, R, g, and thus α for each case. Each MAMOS sample has 1200 simulations for one impact scenario, i.e., 2400 simulations for both scenarios. One issue is that when the transient crater is too large, the computation of the ejecta momentum accumulates numerical errors. This is because Δ and r_0 become extremely small and large, reducing numerical accuracy. To avoid this issue, the algorithm only considers $\Delta_E^* > 20°$, allowing all streamtubes to cover up to about 83% of the entire volume. The $\Delta_E^* > 20°$ constraint likely underestimates the geometric factor. However, such a case makes the geometric factor unrealistic and is rejected by the allowed geometric factor range anyway. For one impact scenario of each sample, this sorting process yields about 85% of simulations that satisfy a geometric factor ranging between −200% and 200 %.

Catastrophic disruption threshold (Q_D^*)

The catastrophic disruption threshold, Q_D^*, defines the specific impact energy per mass required to disperse half of the target material mass, which is given as:

$$Q_D^* = \frac{U^2}{2}\frac{m_{sc}}{M} \tag{17}$$

where m_{sc} is the spacecraft mass, M is the target mass, and U is the spacecraft relative impact speed. In the present study, m_{sc} and U are identical to DART's, and $m_{sc} \ll M$. On the other hand, Q_D^* is also a function of the target radius and strength[90,91]. However, no adequate disruption threshold formula covers the parameter range considered in this study. Accepting this issue, our approach uses two samples with different strengths at different target radii to draw the correlations. In this test, each sample has three bulk density cases, 1000 kg/m^3, 2000 kg/m^3, and 4000 kg/m^3.

The first sample is a target with higher strength[92]. Q_D^* for a high-strength material defines the following equation:

$$Q_D^* = 100^{a_s} \times Q_0 R_{Q_D^*}^{a_s} + 100^{b_s} \times B\rho R_{Q_D^*}^{b_s} \quad (18)$$

where $R_{Q_D^*}$ is the disrupting target radius, ρ is the bulk density, and Q_0, a_s, b, and B are the empirical parameters. Applying an earlier study using Smooth-Particle Hydrodynamics (Bern SPH)[92] yields two high-strength materials. One is a basalt-like target, and the other is a pumice-like target. The parameters used here are based on impact simulations with an impact speed of 5 km/s and a target radius of 1.5 cm[92], given in Supplementary Table 3. Using Equation (18) determines $R_{Q_D^*}$ at kinetic energy imparted by the DART-like impactor.

The earlier targets[92] were 1.5 cm radius, provided with their strengths at this size, Y(1.5 cm). Re-scaling Y(1.5 cm) to Y requires the static failure threshold for a specimen failing at the smallest strain, ϵ_{min}:

$$\epsilon_{min} = (kV_{Q_D^*})^{-\frac{1}{m}} \quad (19)$$

where k and m are the Weibull parameters, given in Supplementary Table 3, and $V_{Q_D^*}$ is the disrupting target volume. Y at a given $R_{Q_D^*}$ is written as:

$$Y = \epsilon_{min} E_s \quad (20)$$

where $E_s = 5.3 \times 10^{10}$ Pa is Young's modulus. Combining these equations with the assumption that the Weinbull parameters and E_s are size-independent yields the relationship between Y and Y(1.5 cm):

$$Y = \left(\frac{V_{Q_D^*}}{1.41 \times 10^{-5}} \right)^{-\frac{1}{m}} Y(1.5cm) \quad (21)$$

The second sample is a cohesionless target[58,93]. Q_D^* for this case gives the equation[90]:

$$Q_D^* = a_g R_{Q_D^*}^{3\mu_g} U^{2-3\mu_g} \quad (22)$$

where a_g and μ_g are empirical parameters, and U is the impact speed (Supplementary Table 3). These quantities are based on Bern SPH simulations using an impact speed range of 3–9 km/s and an impact mass of 500 kg[58]. In this scaling relationship, Y is fixed at 10^{-2} Pa.

Interpolating these two samples yields a correlation between Y and $R_{Q_D^*}$. The interpolation function gives the following power law:

$$Y = \xi R_{Q_D^*}^{\eta} \quad (23)$$

where ξ and η come from the constraint that this scaling function must cross the data samples above. The approach considers two scaling functions: the combination of a pumice-like target and a cohesionless target and that of a basalt target and a cohesionless target[58,92].

Data availability

The used data from DART and LICIACube, including planetary ephemerides, asteroid shape models, and LICIACube images, are available at NASA's Planetary Data System (https://pds-smallbodies.astro.umd.edu/data_sb/missions/dart/index.shtmland https://naif.jpl.nasa.gov/pub/naif/pds/pds4/dart/dart_spice/). The shape models of Didymos and Dimorphos are also available via the Small Body Mapping Tool (SBMT; https://sbmt.jhuapl.edu/) developed by Johns Hopkins Applied Physics Laboratory. The datasets generated in this work have been deposited in the Zenodo database (https://zenodo.org/records/13864402)[94]: Highest-scoring samples that satisfied all conditions for the observed ejecta cone geometry created by the NASA/DART impact on the target asteroid Dimorphos; Asteroid conditions derived from the MAMOS data and geometric factors; Maxwell Z-model parameters determined from the ejecta evolution after the NASA/DART impact. The parameters used for comparison tests, the unit vector quantities for orbital motions of Dimorphos and spacecraft at the DART impact, and the empirical parameters to compute scaling functions of strength and disrupting target radius are provided in the Supplementary Information. Source data, including iSALE-2D simulations, are also provided in this paper. The datasets generated during and/or analyzed during the current study are available from the corresponding author upon request. Source data are provided in this paper.

Code availability

Programs for the Maxwell Z-model approach are available through Zenodo (https://zenodo.org/records/11509782)[95]. The available codes provide geometric factors, given a target's curvature. The published package focuses on comparing the developed Maxwell-Z approach with the iSALE simulations but is used for all the cases analyzed in this study. iSALE-2D is a publicly accessible hydrocode package available upon request (https://isale-code.github.io/).

References

1. Interagency Working Group for Detecting and Mitigating the Impact of Earth-bound Near-Earth Objects. *National Near-Earth Object Preparedness Strategy and Action Plan* (2018).
2. Planetary Defense Interagency Working Group. *National Near-Earth Object Preparedness Strategy and Action Plan* (2023).
3. National Research Council. *Defending Planet Earth: Near-Earth-Object Surveys and Hazard Mitigation Strategies* (The National Academies Press, Washington, DC, 2010).
4. National Academies of Sciences, Engineering, and Medicine. *Origins, Worlds, and Life: A Decadal Strategy for Planetary Science and Astrobiology 2023–2032* (The National Academies Press, Washington, DC, 2022).
5. Holsapple, K. A. & Housen, K. R. Momentum transfer in asteroid impacts. i. theory and scaling. *Icarus* **221**, 875–887 (2012).
6. Rivkin, A. S. et al. The double asteroid redirection test (DART): Planetary defense investigations and requirements. *The Planetary Science Journal* **2**, 173 (2021).
7. Statler, T. S. et al. After dart: Using the first full-scale test of a kinetic impactor to inform a future planetary defense mission. *Planet. Sci. J.* **3**, 244 (2022).
8. Owen, J. M., DeCoster, M. E., Graninger, D. M. & Raducan, S. D. Spacecraft geometry effects on kinetic impactor missions. *Planet. Sci. J.* **3**, 218 (2022).
9. DeCoster, M. E., Rainey, E. S., Rosch, T. W. & Stickle, A. M. Statistical significance of mission parameters on the deflection efficiency of kinetic impacts: Applications for the next-generation kinetic impactor. *Planet. Sci. J.* **3**, 186 (2022).
10. Raducan, S. D., Davison, T. M. & Collins, G. S. The effects of asteroid layering on ejecta mass-velocity distribution and implications for impact momentum transfer. *Planet. Space Sci.* **180**, 104756 (2020).
11. Raducan, S. D., Davison, T. M. & Collins, G. Ejecta distribution and momentum transfer from oblique impacts on asteroid surfaces. *Icarus* **374**, 114793 (2022).

12. Raducan, S. D. et al. Influence of the projectile geometry on the momentum transfer from a kinetic impactor and implications for the DART mission. *Int. J. Impact Eng.* **162**, 104147 (2022).
13. Luther, R. et al. Momentum enhancement during kinetic impacts in the low-intermediate-strength regime: Benchmarking and validation of impact shock physics codes. *Planet Sci. J.* **3**, 227 (2022).
14. Kumamoto, K. M. et al. Predicting asteroid material properties from a dart-like kinetic impact. *Planet. Sci. J.* **3**, 237 (2022).
15. Stickle, A. M. et al. Effects of impact and target parameters on the results of a kinetic impactor: Predictions for the double asteroid redirection test (dart) mission. *Planet. Sci. J.* **3**, 248 (2022).
16. Scheeres, D. J., McMahon, J. W., Jones, B. A. & Doostan, A. Variation of delivered impulse as a function of asteroid shape. In *2015 IEEE Aerospace Conference*, 1–7 (2015).
17. Bruck Syal, M., Michael Owen, J. & Miller, P. L. Deflection by kinetic impact: Sensitivity to asteroid properties. *Icarus* **269**, 50–61 (2016).
18. Feldhacker, J. D. et al. Shape dependence of the kinetic deflection of asteroids. *J. Guid. Control Dyn.* **40**, 2417–2431 (2017).
19. DeCoster, M. E. et al. The relative effects of surface and subsurface morphology on the deflection efficiency of kinetic impactors: Implications for the DART mission. *Planet. Sci. J.* **5**, 21 (2024).
20. Schultz, P. H., Gault, D. E. & Crawford, D. Impacts of hemispherical granular targets: Implications for global impacts. NASA, Washington, Reports of Planetary Geology and Geophysics Program (1986).
21. A'Hearn, M. F. et al. Deep impact: Excavating comet tempel 1. *Science* **310**, 258–264 (2005).
22. Schultz, P. H., Hermalyn, B. & Veverka, J. The deep impact crater on 9p/tempel-1 from stardust-next. *Icarus* **222**, 502–515 (2013).
23. Schultz, P. H. et al. The deep impact oblique impact cratering experiment. *Icarus* **191**, 84–122 (2007).
24. Richardson, J. E., Melosh, H. J., Lisse, C. M. & Carcich, B. A ballistics analysis of the Deep Impact ejecta plume: Determining Comet Tempel 1's gravity, mass, and density. *Icarus* **191**, 176–209 (2007).
25. Ernst, C. M. & Schultz, P. H. Evolution of the deep impact flash: Implications for the nucleus surface based on laboratory experiments. *Icarus* **191**, 123–133 (2007).
26. Arakawa, M. et al. An artificial impact on the asteroid (162173) ryugu formed a crater in the gravity-dominated regime. *Science* **368**, 67–71 (2020).
27. Jutzi, M., Raducan, S. D., Zhang, Y., Michel, P. & Arakawa, M. Constraining surface properties of asteroid (162173) Ryugu from numerical simulations of Hayabusa2 mission impact experiment. *Nat. Commun.* **13**, 7134 (2022).
28. Daly, R. T. et al. Successful kinetic impact into an asteroid for planetary defence. *Nature* **616**, 443–447 (2023).
29. Chabot, N. L. et al. Achievement of the planetary defense investigations of the double asteroid redirection test (dart) mission. *Planet. Sci. J.* **5**, 49 (2024).
30. Daly, R. T. et al. An updated shape model of dimorphos from DART data. *Planet. Sci. J.* **5**, 24 (2024).
31. Thomas, C. A. et al. Orbital period change of Dimorphos due to the DART kinetic impact. *Nature* **616**, 448–451 (2023).
32. Rożek, A. et al. Optical monitoring of the Didymos-Dimorphos asteroid system with the danish telescope around the DART mission impact. *Planet. Sci. J.* **4**, 236 (2023).
33. Jewitt, D., Kim, Y., Li, J. & Mutchler, M. The dimorphos boulder swarm. *Astrophys. J. Lett.* **952**, L12 (2023).
34. Opitom, C. et al. Morphology and spectral properties of the dart impact ejecta with vlt/muse. *Astron. Astrophys.* **671**, L11 (2023).
35. Moreno, F. et al. Characterization of the ejecta from the NASA/DART impact on Dimorphos: Observations and monte carlo models. *Planet. Sci. J.* **4**, 138 (2023).
36. Lolachi, R., Glenar, D. A., Stubbs, T. J. & Kolokolova, L. Optical characterization of the DART impact plume: Importance of realistic ejecta scattering properties. *Planet. Sci. J.* **4**, 24 (2023).
37. Roth, N. X. et al. Alma observations of the dart impact: Characterizing the ejecta at submillimeter wavelengths. *Planet. Sci. J.* **4**, 206 (2023).
38. Murphy, B. P. et al. VLT/MUSE Characterization of Dimorphos ejecta from the DART impact. *Planet. Sci. J.* **4**, 238 (2023).
39. Kim, Y. & Jewitt, D. A single ejection model of the DART/Dimorphos debris trail. *Astrophys. J. Lett.* **956**, L26 (2023).
40. Li, J.-Y. et al. Ejecta from the DART-produced active asteroid Dimorphos. *Nature* **616**, 452–456 (2023).
41. Dotto, E. & Zinzi, A. Impact observations of asteroid Dimorphos via Light Italian CubeSat for imaging of asteroids (LICIACube). *Nat. Commun.* **14**, 3055 (2023).
42. Dotto, E. et al. The Dimorphos ejecta plume properties revealed by LICIACube. *Nature* **627**, 505–509 (2024).
43. Lister, T. et al. Long-term monitoring of Didymos with the LCOGT network and MRO after the DART Impact. *Planet. Sci. J.* **5**, 127 (2024).
44. Moreno, F., Tancredi, G. & Bagatin, A. C. On the fate of slow boulders ejected after DART impact on dimorphos. *Planet. Sci. J.* **5**, 63 (2024).
45. Michel, P. et al. The esa hera mission: Detailed characterization of the dart impact outcome and of the binary asteroid (65803) didymos. *Planet. Sci. J.* **3**, 160 (2022).
46. Cheng, A. F. et al. Momentum transfer from the DART mission kinetic impact on asteroid Dimorphos. *Nature* **616**, 457–460 (2023).
47. Deshapriya, J. D. P. et al. Characterization of the dart impact ejecta plume on dimorphos from liciacube observations. *Planet. Sci. J.* **4**, 231 (2023).
48. Melosh, H. J. *Impact Cratering: A Geologic Process* (Oxford University Press, 1988).
49. Amsden, A. A., Ruppel, H. M. & Hirt, C. W. SALE: a simplified ALE computer program for fluid flow at all speeds. https://doi.org/10.2172/5176006 (1980).
50. Collins, G. S., Melosh, H. J. & Ivanov, B. A. Modeling damage and deformation in impact simulations. *Meteorit. Planet. Sci.* **39**, 217–231 (2004).
51. Wünnemann, K., Collins, G. S. & Melosh, H. J. A strain-based porosity model for use in hydrocode simulations of impacts and implications for transient crater growth in porous targets. *Icarus* **180**, 514–527 (2006).
52. Collins, G. S., Melosh, H. J. & Wünnemann, K. Improvements to the epsilon-alpha porous compaction model for simulating impacts into high-porosity solar system objects. *Int. J. Impact Eng.* **38**, 434–439 (2011).
53. Collins, G. S., Miljković & Davison, T. M. The effect of planetary curvature on impact crater ellipticity. In *European Planetary Science Congress 2013*, vol. 8 (2013).
54. Raducan, S. D. et al. Physical properties of asteroid Dimorphos as derived from the DART impact. *Nat. Astron.* **8**, 445–455 (2024).
55. Cheng, A. F. et al. DART Impact ejecta plume evolution: Implications for Dimorphos. *Planet. Sci. J.* **5**, 118 (2024).
56. Ferrari, F. et al. Morphology of ejecta features from the DART impact on Dimorphos and their implications. *Nat. Commun.* (2024).
57. Stickle, A. M. et al. Dimorphos' material properties and estimates of crater size from the DART impact. *Planet. Sci. J.* **6**, 38 (2025).
58. Raducan, S. D. & Jutzi, M. Global-scale reshaping and resurfacing of asteroids by small-scale impacts, with applications to the DART and hera missions. *Planet. Sci. J.* **3**, 128 (2022).
59. Cline, II, C. J., Cintala, M. J., Anderson, J. L. B. & Bart, G. D. Using controlled impact experiments to understand the effects of cohesive blocks on the cratering processes. In *54th Lunar and Planetary Science Conference 2023*, 1042 (2023).
60. Collins, G. S., Dai, K., Davison, T. M., Raducan, S. D. & Stickle, A. M. The effect of boulder contract on momentum transfer efficiency in

the DART impact. In *54th Lunar and Planetary Science Conference 2023*, 2267 (2023).
61. Farnham1, T. L. et al. Spatial distribution of the boulders in the DART impact ejecta: A 3-D analysis. In *54th Lunar and Planetary Science Conference 2023*, 2426 (2023).
62. Ormö, J. et al. Boulder exhumation and segregation by impacts on rubble-pile asteroids. *Earth Planet. Sci. Lett.* **594**, 117713 (2022).
63. Anderson, J. L. B., Schultz, P. H. & Heineck, J. T. Experimental ejection angles for oblique impacts: Implications for the subsurface flow-field. *Meteorit. Planet. Sci.* **39**, 303–320 (2004).
64. Croft, S. K. Cratering flow fields: Implications for the excavation and transient expansion stages of crater formation. In *Proceedings of the 11th Lunar Planetary Science Conference*, 2437–2378 (1980).
65. Austin, M. G. et al. Z-Model analysis of impact cratering: An overview. In *Proceedings of the 12th Lunar Planetary Science Conference*, 197–205 (1981).
66. Thomsen, J. M., Austin, M. G., Ruhl, S. F., Schultz, P. H. & Orphal, D. L. Calculational investigation of impact cratering dynamics: Early time material motions. In *Proceedings of the 10th Lunar Planetary Science Conference*, 2741–2756 (1979).
67. Thirouin, A. et al. THE MISSION ACCESSIBLE NEAR-EARTH OBJECTS SURVEY (MANOS): FIRST PHOTOMETRIC RESULTS. *Astron. J.* **152**, 163 (2016).
68. Thirouin, A. et al. The mission accessible near-earth objects survey: Four years of photometry. *Astrophys. J. Suppl. Ser.* **239**, 4 (2018).
69. Holsapple, K. A. The scaling of impact processes in planetary sciences. *Annu. Rev. Earth Planet. Sci.* **21**, 333–373 (1993).
70. Hirabayashi, M. et al. Double asteroid redirection test (dart): Structural and dynamic interactions between asteroidal elements of binary asteroid (65803) didymos. *Planet. Sci. J.* **3**, 140 (2022).
71. Hirabayashi, M. Failure modes and conditions of a cohesive, spherical body due to YORP spin-up. *Mon. Not. R. Astron. Soc.* **454**, 2249–2257 (2015).
72. McInnes, C. R. Deflection of near-earth asteroids by kinetic energy impacts from retrograde orbits. *Planet. Space Sci.* **52**, 587–590 (2004).
73. Lubin, P. & Cohen, A. N. Asteroid interception and disruption for terminal planetary defense. *Adv. Space Res.* **71**, 1827–1839 (2023).
74. Naidu, S. P. et al. Orbital and physical characterization of asteroid dimorphos following the DART impact. *Planet. Sci. J.* **5**, 74 (2024).
75. Pravec, P. et al. Rotational lightcurves of Dimorphos and constraints on its post-DART impact spin state. *Icarus* **418**, 116138 (2024).
76. Nakano, R. et al. NASA's Double asteroid redirection test (DART): Mutual orbital period change due to reshaping in the near-earth binary asteroid system (65803) didymos. *Planet. Sci. J.* **3**, 148 (2022).
77. Nakano, R. et al. Dimorphos's orbit period change and attitude perturbation due to its reshaping after the dart impact. *Planet. Sci. J.* **5**, 133 (2024).
78. Chabot, N., Adams, E., Rivkin, A. & Kalirai, J. DART: Latest results from the Dimorphos impact and a look forward to future planetary defense initiatives. *Acta Astronaut.* **220**, 118–125 (2024).
79. Maxwell, D. E. Simple Z model for cratering, ejection, and the overturned flap. In *Impact and Explosion Cratering. Planetary and Terrestrial Implications* 1003–1008 (1977).
80. Barnhart, C. J. & Nimmo, F. Role of impact excavation in distributing clays over Noachian surfaces. *J. Geophys. Res. Planets* **116**, https://doi.org/10.1029/2010JE003629 (2011).
81. Nakano, R. & Hirabayashi, M. Mass-shedding activities of asteroid (3200) Phaethon enhanced by its rotation. *Astrophys. J. Lett.* **892**, L22 (2020).
82. Hirabayashi, M. et al. Spin-driven evolution of asteroids' top-shapes at fast and slow spins seen from (101955) bennu and (162173) ryugu. *Icarus* **352**, 113946 (2020).
83. Robin, C. Q. et al. Mechanical properties of rubble pile asteroids (Dimorphos, Itokawa, Ryugu, and Bennu) through surface boulder morphological analysis. *Nat. Commun.* **15**, 6203 (2024).
84. Warner, B., Harris, A. & Pravec, P. Asteroid lightcurve database (LCDB) bundle V3.0, https://doi.org/10.26033/7h40-8s80 (2019).
85. Tillotson, H. J. Metallic equations of state for hypervelocity impact. *General Atomic Rep.***GA-3216**, 141 (1962).
86. Johnson, G. R. & Cook, W. H. A constitutive model and data for metals subjected to large strains, high strain rates and high temperatures. In *Proceedings of the 7th International Symposium on Ballistics, The Hague* 541–547 (1983).
87. Benz, W. & Asphaug, E. Catastrophic disruptions revisited. *Icarus* **142**, 5–20 (1999).
88. Consolmagno, G. J., Britt, D. T. & Macke, R. J. The significance of meteorite density and porosity. *Geochemistry* **68**, 1–29 (2008).
89. Housen, K. R. & Holsapple, K. A. Ejecta from impact craters. *Icarus* **211**, 856–875 (2011).
90. Housen, K. R. & Holsapple, K. A. On the fragmentation of asteroids and planetary satellites. *Icarus* **84**, 226–253 (1990).
91. Housen, K. R. & Holsapple, K. A. Scale effects in strength-dominated collisions of rocky asteroids. *Icarus* **142**, 21–33 (1999).
92. Jutzi, M., Michel, P., Benz, W. & Richardson, D. C. Fragment properties at the catastrophic disruption threshold: The effect of the parent body's internal structure. *Icarus* **207**, 54–65 (2010).
93. Raducan, S. D. et al. Lessons learned from NASA's DART impact about disrupting rubble-pile asteroids. *Planet. Sci. J.* **5**, 79 (2024).
94. Hirabayashi, M. NASA/DART impact-induced ejecta cone geometry measurement and Maxwell-Z model parameters. https://zenodo.org/records/13864402 (2024).
95. Hirabayashi, M. Maxwell Z-model approach to compute the geometric factors for kinetic deflection on curvature. https://zenodo.org/records/11509782 (2024).
96. Barnouin, O. et al. The geology and evolution of the Near-Earth binary asteroid system (65803) Didymos. *Nat. Commun.* **15**, 6202 (2024).

Acknowledgements

This work was supported by the DART mission, NASA Contract No. 80MSFC20D0004. M.H. acknowledges NASA/HERA-PSP (80NSSC24K1434). This work was supported by the Italian Space Agency (ASI) within the LICIACube project (ASI-INAF agreement n. 2019-31-HH.0 and its extension 2019-31-HH.1-2022). This work is partially supported by NASA through grant HSTGO-16674 from the Space Telescope Science Institute, which is operated by the Association of Universities for Research in Astronomy, Inc., under NASA contract NAS 5-26555. Portions of this work were performed by Lawrence Livermore National Laboratory under DOE contract DE-AC52-07NA27344. LLNL-JRNL-853920. S.D.R. and M.J. acknowledge support from the Swiss National Science Foundation (project number 200021 207359). Work of E.G.F., S.P.N., and S.R.C. was carried out at the Jet Propulsion Laboratory, California Institute of Technology, under a contract with the National Aeronautics and Space Administration (80NM0018D0004). R.M. acknowledges funding from a NASA Space Technology Graduate Research Opportunities (NSTGRO) award, NASA contract No. 80NSSC22K1173. H.F.A. was supported by the French government through the UCA J.E.D.I. Investments in the Future project managed by the National Research Agency (ANR) with the reference number ANR-15-IDEX-01. P.M. acknowledges funding support from the French Space Agency CNES and The University of Tokyo. G.T. acknowledges financial support from project FCE-1-2019-1-156451 of the Agencia Nacional de Investigación e Innovación ANII and Grupos I + D 2022 CSIC-Udelar (Uruguay). The work by J.O., S.D.R., and G.S.C. was supported by Grant PID2021-125883NB-C22 by the Spanish Ministry of Science and Innovation/State Agency of Research MCIN/AEI/10.13039/501100011033 and by "ERDF A way of making Europe." J.O., I.H., S.D.R., and M.J. were

supported by the Spanish Research Council (CSIC) support for international cooperation: I-LINK project ILINK22061. S.R.S. acknowledges support from the DART Participating Scientist Program, grant no. 80NSSC22K0318. R.L., D.G., and T.S. acknowledge support by the NASA/GSFC Internal Scientist Funding Model (ISFM) Exospheres, Ionospheres, Magnetospheres Modeling (EIMM) team, and the NASA Solar System Exploration Research Virtual Institute (SSERVI). R.L. and D.G. acknowledge work done through the Center for Research and Exploration in Space Science and Technology (CRESST-II) supported by NASA award number 80GSFC24M0006. This research was supported in part through research cyberinfrastructure resources and services provided by the Partnership for an Advanced Computing Environment (PACE) at the Georgia Institute of Technology. The authors also acknowledge Mark Cintala for his helpful comments on this manuscript. J.Y.L.'s work was mostly performed at PSI before he moved to SYSU.

Author contributions

M.H. led this project, developed techniques, conducted analysis and data assessment, and created the full story. S.D.R conducted iSALE simulations and gave interpretations of the DART impacts on Dimorphos. J.M.S. and T.L.F. offered overall guidance on this project and gave interpretations of the ejecta plume evolution. J.D.P.D. shared insights into ejecta plume geometry based on LICIACube data. J.Y.L. shared insights into ejecta plume geometry based on the interpretations of HST data. G.T. offered interpretations of ejecta plume geometry. S.R.C., R.T.D., C.M.E., I.G., P.H.H., S.P.N., H.N., E.E.P, C.D.W., and A.Z. developed the mission-driven data necessary for this work. H.F.A., B.W.B., M.B.S., G.S.C., T.M.D., M.E.D., M.J., K.M.K., N.A.M., J.R.L., and S.R.S. assessed the techniques used in this work for their validity. P.A.A., O.S.B., N.L.C., A.F.C., E.D., E.G.F., P.M., D.C.R., A.S.R., A.M.S., and C.A.T. are the leadership members of DART, LICIACube, and Hera, performing project management and execution and giving advice and comments on this work from mission level. R.T.D., B.W.B., M.B.S., J.R.L., and N.L.C. also gave advice on how to connect this work with planetary defense. J.B., J.R.B., M.D.'O., V.D.C., E.M.E., S.Ie., G.I., S.Iv., A.L., D.M., M.P., P.P., S.P., G.P., A.R., P.T., F.T., M.Z., and G.Z. contributed to LICIACube data analysis and advised on how to interpret the data. F.F., D.A.G., I.H., S.A.J., Ö.K., M.L., R.L., M.P.L., R.M., F.M., C.C.M., A.M., R.N., J.O., P.S., C.B.S., S.S., and T.J.S. added scientific inputs to the present study. All contributed to the manuscript development.

Competing interests

The authors declare no competing interests.

Additional information

Supplementary information The online version contains supplementary material available at https://doi.org/10.1038/s41467-025-56010-w.

Correspondence and requests for materials should be addressed to Masatoshi Hirabayashi.

Peer review information *Nature Communications* thanks the anonymous reviewers for their contribution to the peer review of this work. A peer review file is available.

Masatoshi Hirabayashi[1] ✉, Sabina D. Raducan[2], Jessica M. Sunshine[3], Tony L. Farnham[3], J. D. P. Deshapriya[4], Jian-Yang Li[5,6], Gonzalo Tancredi[7], Steven R. Chesley[8], R. Terik Daly[9], Carolyn M. Ernst[9], Igor Gai[10], Pedro H. Hasselmann[4], Shantanu P. Naidu[8], Hari Nair[9], Eric E. Palmer[6], C. Dany Waller[9], Angelo Zinzi[11,12], Harrison F. Agrusa[3,13], Brent W. Barbee[14], Megan Bruck Syal[15], Gareth S. Collins[16], Thomas M. Davison[16], Mallory E. DeCoster[9], Martin Jutzi[2], Kathryn M. Kumamoto[15], Nicholas A. Moskovitz[17], Joshua R. Lyzhoft[14], Stephen R. Schwartz[6,18], Paul A. Abell[19], Olivier S. Barnouin[9], Nancy L. Chabot[9], Andrew F. Cheng[9], Elisabetta Dotto[4], Eugene G. Fahnestock[8], Patrick Michel[13,20], Derek C. Richardson[3], Andrew S. Rivkin[9], Angela M. Stickle[9], Cristina A. Thomas[21], Joel Beccarelli[22], John R. Brucato[23], Massimo Dall'Ora[24], Vincenzo Della Corte[24], Elena Mazzotta Epifani[4], Simone Ieva[4], Gabriele Impresario[11], Stavro Ivanovski[25], Alice Lucchetti[22], Dario Modenini[10], Maurizio Pajola[22], Pasquale Palumbo[26], Simone Pirrotta[11], Giovanni Poggiali[23], Alessandro Rossi[27], Paolo Tortora[10], Filippo Tusberti[22], Marco Zannoni[10], Giovanni Zanotti[28], Fabio Ferrari[28], David A. Glenar[14,29], Isabel Herreros[30], Seth A. Jacobson[31], Özgür Karatekin[32], Monica Lazzarin[33], Ramin Lolachi[14,29], Michael P. Lucas[34], Rahil Makadia[35], Francesco Marzari[33], Colby C. Merrill[36], Alessandra Migliorini[26], Ryota Nakano[1], Jens Ormö[30], Paul Sánchez[37], Cem Berk Senel[32,38], Stefania Soldini[39] & Timothy J. Stubbs[14]

[1]Georgia Institute of Technology, Atlanta, GA, USA. [2]University of Bern, Bern, Switzerland. [3]University of Maryland, College Park, MD, USA. [4]INAF-Osservatorio Astronomico di Roma, Rome, Italy. [5]Sun Yat-sen University, Zhuhai, China. [6]Planetary Science Institute, Tucson, AZ, USA. [7]Facultad de Ciencias, UdelaR,

Montevideo, Uruguay. [8]Jet Propulsion Laboratory, California Institute of Technology, Pasadena, CA, USA. [9]Johns Hopkins University Applied Physics Laboratory, Laurel, MD, USA. [10]Alma Mater Studiorum - Università di Bologna, Forlì, Italy. [11]Agenzia Spaziale Italiana (ASI), Rome, Italy. [12]Space Science Data Center, ASI, Rome, Italy. [13]Universitê Côte d'Azur, Observatoire de la Côte d'Azur, CNRS, Laboratoire Lagrange, Nice, France. [14]NASA/Goddard Space Flight Center, Greenbelt, MD, USA. [15]Lawrence Livermore National Laboratory, Livermore, CA, USA. [16]Imperial College London, London, UK. [17]Lowell Observatory, Flagstaff, AZ, USA. [18]Universidad de Alicante, Alicante, Spain. [19]NASA Johnson Space Center, Houston, TX, USA. [20]The University of Tokyo, Tokyo, Japan. [21]Northern Arizona University, Flagstaff, AZ, USA. [22]INAF-Osservatorio Astronomico di Padova, Padova, Italy. [23]INAF-Osservatorio Astronomico di Arcetri, Firenze, Italy. [24]INAF-Osservatorio Astronomico di Capodimonte, Napoli, Italy. [25]INAF-Osservatorio Astronomico di Trieste, Trieste, Italy. [26]INAF-Istituto di Astrofisica e Planetologia Spaziali, Rome, Italy. [27]IFAC-Istituto di fisica applicata Nello Carrara, Sesto Fiorentino, Italy. [28]Politecnico di Milano, Milano, Italy. [29]University of Maryland Baltimore County, Baltimore, MD, USA. [30]Centro de Astrobiologia (CAB), CSIC-INTA, Madrid, Spain. [31]Michigan State University, East Lansing, MI, USA. [32]Royal Observatory of Belgium, Brussels, Belgium. [33]Università di Padova, Padova, Italy. [34]Florida Space Institute, Orlando, FL, USA. [35]University of Illinois at Urbana-Champaign, Urbana, IL, USA. [36]Cornell University, Ithaca, NY, USA. [37]University of Colorado Boulder, Boulder, CO, USA. [38]Vrije Universiteit Brussel, Brussels, Belgium. [39]University of Liverpool, Liverpool, UK. ✉e-mail: thirabayashi@gatech.edu